

Article

# Application of S-Transform in ISAR Imaging

Bo Zang, Mingzhe Zhu \* , Xianda Zhou and Lu Zhong

School of Electronic Engineering, Xidian University, Xi'an 710126, China; bzang@mail.xidian.edu.cn (B.Z.); zhoxianda999@gmail.com (X.Z.); zhonglu@protonmail.com (L.Z.)

\* Correspondence: zhuzm@mail.xidian.edu.cn

Received: 25 April 2019; Accepted: 11 June 2019; Published: 14 June 2019



**Abstract:** In inverse synthetic aperture radar (ISAR) imaging, time-frequency analysis is the basic method for processing echo signals, which are reflected by the results of time-frequency analysis as each component changes over time. In the time-frequency map, a target's rigid body components will appear as a series of single-frequency signals in the low-frequency region, and the micro-Doppler components generated by the target's moving parts will be distributed in the high-frequency region with obvious frequency modulation. Among various time-frequency analysis methods, S-transform is especially suitable for analyzing these radar echo signals with micro-Doppler (m-D) components because of its multiresolution characteristics. In this paper, S-transform and the corresponding synchrosqueezing method are used to analyze the ISAR echo signal and perform imaging. Synchrosqueezing is a post-processing method for the time-frequency analysis result, which could retain most merits of S-transform while significantly improving the readability of the S-transformation result. The results of various simulations and actual data will show that S-transform is highly matched with the echo signal for ISAR imaging: the better frequency-domain resolution at low frequencies can concentrate the energy of the rigid body components in the low-frequency region, and better time resolution at high frequencies can better describe the transformation of the m-D component over time. The combination with synchrosqueezing also significantly improves the effect of time-frequency analysis and final imaging, and alleviates the shortcomings of the original S-transform. These results will be able to play a role in subsequent work like feature extraction and parameter estimation.

**Keywords:** time-frequency analysis; S-transformation; ISAR; micro-Doppler; synchrosqueezing

## 1. Introduction

In inverse synthetic aperture radar (ISAR) imaging, to obtain the final image, two steps of Fourier transform are necessary for the original echo signal. Through the Fourier transform, the periodic characteristics of the time domain signal are found and reflected in the frequency domain. With the periodic characteristics in different dimensions combined with the appropriate resolution, the shape information of the target can be obtained [1].

In these radar echo signals, the rigid body part of the target and the moving part will produce two types of component. The latter will be referred to as the micro-Doppler (m-D) component with frequency modulation, which may generate from rotation of propellers or rotor wings on plane, surface vibration caused by engine, and swinging arms when human walk may cause the m-D effect [2,3].

The m-D component usually interferes with the final imaging result, but on the other hand, it can also be used for feature extraction and parameter estimation of the target, which is useful information in subsequent work [4]. However, in the face of such components, the simple Fourier transform cannot analyze the transformation of their frequency domain characteristics with time. For this reason, time-frequency analysis, which was born to characterize the transformation of signals in the frequency



where  $A$  is the amplitude of the echo signal,  $T_p$  is the pulse width,  $\gamma$  is the modulation rate,  $c$  is the velocity of light,  $\lambda$  is the wavelength of carrier frequency, and  $R_\Delta(t_m) = R - R_0$  is the distance difference from scattering point  $Q$  to the radar displaced phase center and reference point  $O$ .  $f_r$  and  $t_m$  correspond to the frequency domain and slow time of the pulse compression result, respectively.

For the rigid scattering point  $Q$ ,

$$R_{\Delta Q}(t_m) = \sqrt{R_0^2 + r_Q^2 - 2R_0r_Q \cos(\theta(t_m) + \theta_{Q0} + \frac{\pi}{2})} \approx r_Q \sin(\theta_Q(t_m) + \theta_{Q0}), \tag{2}$$

where  $r_Q$  is the distance from the rigid rotation center to point  $Q$ ,  $\theta_{Q0}$  is the angle between the  $X$  axis and  $OQ$  in coordinate  $XOY$ , and  $\theta_Q(t_M) = \omega t_m$ . Based on the assumption of the uniform circular motion for point  $Q$ , it is centered at  $O$  with angular velocity  $\omega_Q$  in the coherent accumulative time.

Since the accumulation on cross-range is very small here, it has  $\cos(\theta_Q(t_m)) \approx 1$ ,  $\sin(\theta_Q(t_m)) \approx 0$ . The Doppler frequency of  $Q$  is given by

$$f_{dQ} = \frac{2}{\lambda} \frac{dR_{\Delta Q}(t_m)}{dt_m} \approx \frac{2}{\lambda} \omega_Q x_{Q0}. \tag{3}$$

For high-speed rotating scattering point  $P$  on target, while it has the same rotation center to point  $O$  as  $Q$ , another rotation with center point  $o'$  of moving parts makes it different. As in Figure 1, it has

$$R_{\Delta P} \approx r_{o'} \sin(\theta_{o'}(t_m) + \theta_{o'0}) + r_{rot} \sin(\theta_p(t_m) + \theta_{p0}), \tag{4}$$

where  $r_{o'}$  is the distance from  $o'$  to  $O$ ,  $\theta_{o'0}$  is the angle between the  $X$  axis and  $Oo'$  at zero time, and they have  $\theta_{o'}(t_m) = \omega t_m$ . Similarly,  $r_{rot}$  is the radius of the rotation of  $P$ ,  $\theta_{p0}$  is the angle between the  $X$  axis and  $o'P$  at zero time, and they are related as  $\theta_p(t_m) = \omega_p t_m$ . In comparison to  $Q$ , one more rotation of  $P$  introduces a term of sinusoidal modulation to it's Doppler frequency:

$$f_{dP} = \frac{2}{\lambda} \frac{dR_{\Delta P}(t_m)}{dt_m} = \frac{2}{\lambda} \frac{d[r_{o'} \sin(\theta_{o'}(t_m) + \theta_{o'0}) + r_{rot} \sin(\theta_p(t_m) + \theta_{p0})]}{dt_m} \approx \frac{2}{\lambda} [x_{o'} \omega_Q + r_{rot} \cos(\theta_p(t_m) + \theta_{p0}) \omega_P], \tag{5}$$

which is called m-D information.

In the above model of the m-D effect, in coherent accumulative time, rigid parts appear as superpositions of sinusoidal waves in ISAR's cross-range. Then, moving parts add modulation. When there are  $Nr$  scattering points in rigid parts, and  $Nm$  in moving parts, the echo signal could be written as

$$\begin{cases} s = s_1 + s_2 \\ s_1 = \sum_{p=1}^{Nr} A_{1p} \exp(j2\pi f_{1p}t) \\ s_2 = \sum_{q=1}^{Nm} A_{2q} \exp(j2\pi(f_{2q}t + \lambda_q \sin(\omega_q t))), \end{cases} \tag{6}$$

where  $s_1$  represents the components from rigid parts, and  $A_{1p}$  and  $f_{1p}$  are the amplitude and frequency of the cross-range Doppler signal for the  $p$ th scattering point, respectively.  $s_2$ ,  $A_{2q}$  and  $f_{2q}$  have the same meaning for moving parts, and  $\lambda_q \sin(\omega_q t)$  is the m-D information.

Figure 2 shows the process of ISAR imaging.

Originally, in the dotted line parts of Figure 2, signals from different range cells only need to do the Fourier transform then arrange results in order, the imaging result would then be obtained. In the frequency domain of those signals, the energy of the sinusoidal frequency modulated (FM) component

brought by moving parts will be distributed in a range where the spectrum is larger than the rigid body component. In the final imaging results, they seemed to be unwanted interference information relative to the rigid body part. The Fourier transform only shows the distribution of these interferences in the frequency domain but does not indicate the information of these m-D components over time. In Figure 1, Fourier transform is replaced by time-frequency analysis, and the m-D information is reflected in a more specific form on the time-frequency plane.

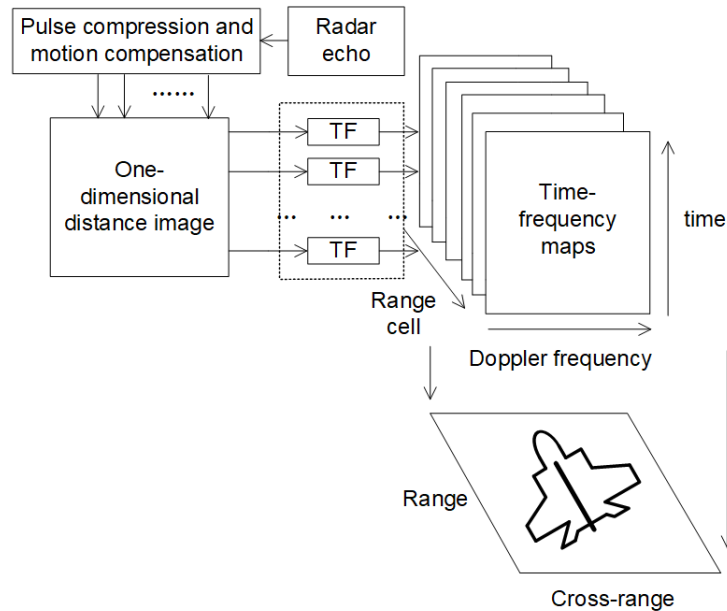


Figure 2. The process of ISAR time-frequency imaging.

### 3. Time-Frequency Analysis and S-Transform

Generally, time-frequency analysis methods can be divided into two categories: one-order time-frequency transform and second-order time-frequency distribution [12]. Although the latter works much better than the former for the single-component signals, it would bring cross-terms that are inconvenient to handle when processing multicomponent signals. As mentioned above, the signals used for imaging in this paper are multicomponent (6), so the time-frequency distribution method is not desirable. Thus, here we will start with the most basic short-time Fourier transform (STFT) in the one-order time-frequency transform.

The multicomponent (MC) FM signal is considered as

$$x(t) = \sum_{m=1}^M A_m \cdot \exp(j(\phi_m(t))), \tag{7}$$

here  $\phi_m(t)$  is the phase function of the  $m$ th signal, and  $A_m$  is the amplitude.

As the signal is inserted into the time-frequency plane by short time Fourier transform (STFT), we have

$$STFT(t, f) = \int_{-\infty}^{+\infty} x(\tau)w(\tau - t)e^{-2i\pi f\tau} d\tau, \tag{8}$$

where  $w(t)$  is usually a Gaussian window function with fixed parameters. This would bring a fixed time-frequency resolution to the analysis result. Even if it is adjusted, it is difficult to get the overall optimality.

Similarly, the S-transform is defined as

$$ST_x(t, f) = \int_{-\infty}^{+\infty} x(\tau)h(\tau - t, f)e^{-2i\pi f\tau} d\tau, \tag{9}$$

and it holds a variable Gaussian window function.

$$h(t, f) = \frac{|f|}{\sqrt{2\pi}} e^{-\frac{f^2 t^2}{2}} \tag{10}$$

For the component located in the low frequency region, the window function is longer and has better frequency resolution. The high-frequency area is the opposite, with better time resolution.

This feature matches the radar echo signal form (6) used for imaging in this paper: The better frequency resolution at low frequencies concentrates the energy of the rigid body component, while the better time resolution at high frequencies depicts the variation of the m-D component over time.

All of the above would make it possible for ST to get better results than STFT overall. In application, to keep the frequency resolution of the high frequency region, a lower bound should be set for the window length.

$$h(t, f) = \begin{cases} \frac{|f|}{\sqrt{2\pi}} e^{-\frac{f^2 t^2}{2}} & , f \leq f_{max} \\ \frac{|f_{max}|}{\sqrt{2\pi}} e^{-\frac{f_{max}^2 t^2}{2}} & , f > f_{max} \end{cases} \tag{11}$$

#### 4. Synchrosqueezing Method

The results obtained from ST analysis are still somewhat insufficient: the energy would spread in the frequency direction of the high-frequency part, which affects the readability of the time-frequency map. Here, the synchrosqueezing method will be introduced for this problem. It is a post-processing method for time-frequency analysis results. The energy is compressed from the frequency direction, the final map is significantly improved, and the beneficial characteristics of the ST can be preserved.

If we consider a harmonic signal  $x(t) = Ae^{i2\pi f_1 t}$ , its Fourier Transform is shown as

$$X(f) = 2\pi A\delta(f - f_1), \tag{12}$$

where  $\delta$  is the Dirac-delta function. Hence, the S-transform of  $x(t)$  can be expressed as

$$ST_x(t, f) = Ae^{-\frac{2\pi^2(f_1-f)^2}{f^2}} e^{2\pi i(f_1-f)t}. \tag{13}$$

This illustrates that  $e^{-\frac{2\pi^2(f_1-f)^2}{f^2}} e^{2\pi i(f_1-f)t}$  are distributed into the ambiguity area in (9). Ideally, the frequency of  $x(t)$  is concentrated around  $f_1$ . In practice, the energy of  $ST_x(t, f)$  spreads out in a range of frequency. To eliminate the effect of modulated items, in the ST spectrum, the signal can calculate the instantaneous frequency (IF) whenever  $ST_x(t, f) \neq 0$  for any  $(t, f)$  by

$$\hat{\omega}_x(t, f) = f + \text{Im}\left(\frac{\partial_t ST_x(t, f)}{ST_x(t, f)}\right). \tag{14}$$

The form of the IF is suitable for S-transform [13]. Here,  $\partial_t ST_x(t, f)$  means  $ST_x(t, f)$  is partial to  $t$ . By using (9), we can obtain  $\hat{\omega} = f_1$ . The multicomponent signals can be defined as a superposition of AM-FM components

$$x(t) = \sum_{K=1}^N A_K(t)e^{2\pi i\phi_K(t)}, \tag{15}$$

where the  $A_K$  and  $\phi_k$  are, respectively, time-varying amplitude and phase functions satisfying  $A_K(t) > 0, \phi'_k(t) > 0$  and  $\phi'_{k+1}(t) > \phi'_k(t)$  for any  $t$ . The goal is to recover the instantaneous frequencies  $\phi'_k$  and the instantaneous amplitudes  $A_K(t)$ . If there is some distance between the different components, i.e.,

$$\phi'_{k+1}(t) - \phi'_k(t) > 2\Delta, \tag{16}$$

where  $\Delta \in (0,1)$ , it is called the well-separated multicomponent signal.  $\hat{\omega}(t, f)$  can also perform effectively for IF estimation [14].

#### 4.1. Synchrosqueezing S-Transform

Before introducing synchrosqueezing transform, it is necessary to revisit the reassignment technique (RM) [15]. The aim of RM is to sharpen the time frequency (TF) representation. There are two meaningful quantities that are called reassignment operators,  $\hat{\omega}_x(t, f)$  and  $\hat{t}_x(t, f)$ . The former is the same as Equation (14) and the latter is defined as

$$\hat{t}_x(t, f) = t - \text{Re}\left(\frac{\partial_f ST_x(t, f)}{2i\pi ST_x(t, f)}\right). \tag{17}$$

Here,  $\partial_f ST_x(t, f)$  means  $ST_x(t, f)$  is partial to  $f$ . While RM as a useful post-processing technique that moves the coefficients according to the map  $(t, f) \rightarrow (\hat{t}_x, \hat{\omega}_x)$  in the TF plane, no mode reconstruction method is available.

Synchrosqueezing transform was originally introduced for analyzing auditory signals in [16] and developed further in [8]. It can be viewed as a special reassignment method. The coefficients are reassigned according to the map  $(t, f) \rightarrow (t, \hat{\omega}_x(t, f))$ , making it remain invertible. The synchrosqueezing S-transform (SSST) is defined as follows:

$$\begin{aligned} SSST(t, \omega) &= \int_{\{\omega_l | |ST_x(t, \omega_l)| > \gamma\}} ST_x(t, \omega_l) \delta(\omega - \hat{\omega}_x(t, \omega_l)) d\omega_l, \end{aligned} \tag{18}$$

where  $\gamma$  is an adjustable threshold.

By squeezing the frequency components within a certain range of instantaneous frequency, an energy-concentrated TF representation can be obtained. Then, the reconstruction of the original signal is computed by

$$x(t) = \frac{1}{C_h} \int_{-\infty}^{+\infty} SSST(t, \omega) \frac{d\omega}{\omega}, \tag{19}$$

where  $C_h = \text{Re}(C_\varphi C_\psi), C_\varphi = e^{-i2\pi f t^2}$ , and  $C_\psi = \frac{1}{2} \int_0^{+\infty} \overline{\hat{\psi}(\xi)} \frac{1}{\xi} d\xi$ .  $\overline{\hat{\psi}(\xi)}$  is the complex conjugate of the Fourier transform of the mother wavelet  $\psi(t) = \frac{1}{\sqrt{w\pi}} e^{-\frac{t^2}{2}} e^{i2\pi t}$ .

More details of the proof can be found in [13].

#### 4.2. Second-Order Synchrosqueezing S-Transform

Although SST gives a good TF representation and mode reconstruction for multicomponent signals, it is restricted to analysis signals made of weakly modulated modes [17]. For a mode  $x(t) = A_K(t)e^{2\pi i\phi_k}$ , only when  $\phi''_k(t)$  is approximate to zero or very small compared to  $\phi'_k(t)$ , the instantaneous frequency estimation  $\hat{\omega}(t, f)$  is close to  $\phi'_k(t)$ . When considering the strong frequency-modulated signal, for instance a quadratic chirp, the  $\phi''_k$  is no longer negligible.

In order to deal with highly modulated signals like m-D components, second-order synchrosqueezing S-transform (SST2) was introduced by a more accurate IF estimate, based on

the second-order operator. The operator corresponds to the second-order derivatives of phase  $Re\{\hat{q}_x(t, f)\} = \phi_k''(t)$ . The second-order local complex modulation operator  $\hat{q}_x(t, f)$  is defined as

$$\begin{aligned} \hat{q}_x(t, f) &= \frac{\partial_t \hat{\omega}_x(t, f)}{\partial_t \hat{t}_x(t, f)} \\ &= \frac{ST_x \partial_{tt}^2 ST_x - (\partial_t ST_x)^2}{2i\pi ST_x^2 - ST_x \partial_{tf}^2 ST_x + \partial_t ST_x \partial_f ST_x} \end{aligned} \tag{20}$$

where  $\partial_{tt}^2 ST_x$  represents  $ST_x$  to  $t$  for second-order partial derivatives, and  $\partial_{tf}^2 ST_x$  means that  $ST_x$  is partial to  $t$  and then partial to  $f$ . Owing to the operator, a more precise IF estimate  $\hat{\omega}_x^{(2)}(t, f)$  can be obtained as

$$\hat{\omega}_x^{(2)}(t, f) = \begin{cases} \hat{\omega}_x + f + \hat{q}_x(2t - \bar{t}), & \partial_t \hat{t}_x \neq 0 \\ \hat{\omega}_x + f, & \partial_t \hat{t}_x = 0. \end{cases} \tag{21}$$

Then, the second-order synchrosqueezing S-transform (SSST2) is modified by replacing  $\hat{\omega}_x$  by  $\hat{\omega}_x^{(2)}$  in (15).

$$\begin{aligned} SSST2(t, \omega) &= \int_{\{\omega_l, |ST_x(t, \omega_l)| > \gamma\}} ST_x(t, \omega_l) \delta(\omega - \hat{\omega}_x^{(2)}(t, \omega_l)) d\omega_l \end{aligned} \tag{22}$$

### 5. Numerical Experimental Results

For the sake of clarity, the abbreviations used below will be detailed here. They are S-transform (ST), short-time Fourier transform (STFT), synchrosqueezing transform (SST), synchrosqueezing S-transform (SSST), and second-order synchrosqueezing S-transform (SSST2).

In this section, the simulation experiment with adjustable parameters will be given first. Results are compared using different time-frequency analysis methods. Subsequently, the actual ISAR signal is also tested.

First, ISAR data is simulated on the helicopter miniaturization model in Figure 3. The simulation parameters are shown in Table 1. Its resolution will be more than enough for the target. Three different propeller speeds are set, which plays a decisive role in the performance of the m-D component.

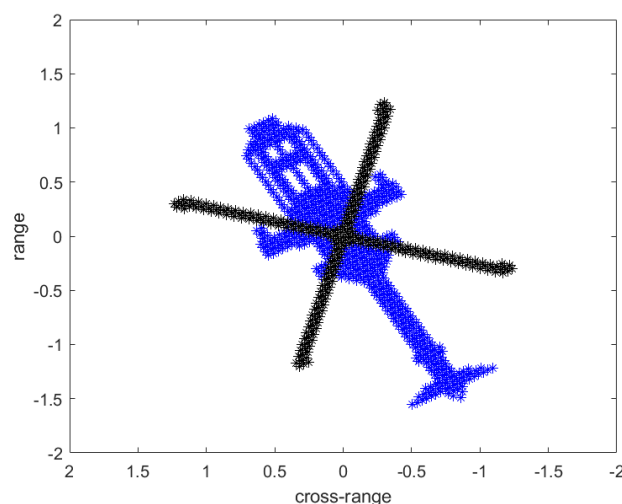


Figure 3. ISAR geometric model.



**Table 1.** Simulation parameters.

Parameter/Variable	Value	Parameter/Variable	Value
Center wavelength	$10.6 \times 10^{-6}$ m	Target size	$2.5 \text{ m} \times 2.5 \text{ m}$
Transmitting bandwidth	$20 \times 10^9$ Hz	Velocity	100 m/s
Pulse repetition frequency	$7 \times 10^3$ Hz	Main rotor speed	20/10/5 r/s
Coherent accumulation time	0.1 s	Route angle relative to radar ray	$30^\circ$
Transmitting width	1 $\mu$ s	Imaging distance	10 Km
Range sampling points	620	Cross-range sampling points	700

In Figure 4a,c, the imaging results using STFT and ST are respectively shown. Although both of them roughly represent the outline of the target rigid body part due to the setting of the experimental parameters, it is obvious that the ST subsection is more accurate and reflects some details. The reason can be seen from the time-frequency analysis results of the single distance unit (300th) using two methods: for the rigid body component, ST can obtain a more gradual result for the low-frequency part, while it would jitter in the STFT (Figure 4b,d).

After applying the synchrosqueezing method, the imaging effects of both methods have been significantly improved. The SST imaging result (Figure 4e) is more concentrated, and the contour of the target becomes clearer. In the time-frequency map, the energy is concentrated in the low-frequency part, but the jitter of the rigid body component still exists (Figure 4f).

For relatively clear ST imaging results, the SSST changes are more reflected in the further depiction of the details (Figure 4g). Since the application of the ST changes the energy distribution of the signal in the frequency domain, the difference in energy between the rigid body imaging result and the m-D information is not as sharp as the SST result. But this also makes the m-D component not too weak (Figure 4h). In addition, in the results of SSST, the readability of the m-D component is also significantly improved, although this should mainly be attributed to ST. But the effect of the original ST in the high-frequency part is not ideal (Figure 4b).

When the rotational speed is increased to 10 r/s and 20 r/s, the same analysis results as those of Figure 4 are also correspondingly placed in Figures 5 and 6.

The difference between these results is the same as when the rotating speed is 5 r/s, but the m-D component brings more interference than before, which makes the imaging result blurred (Figures 5a,c,e,g and 6a,c,e,g).

The characteristics of the results of each time-frequency analysis are not significantly different from the previous ones; the jitter range of the rigid body components of STFT and SST seems to be larger (Figures 5b,f and 6b,f). In the results of ST and SSST, the energy is more distributed at high frequencies (Figure 5c,d,g,h). These changes become more pronounced after increasing the rotational speed to 20 r/s (Figure 6c,d,g,h).

After the second-order synchrosqueezing is further applied (Figure 7), it mainly affects the time resolution of the m-D separation in each time-frequency map (Figure 7b,d,f). This is easier to observe in the zoomed red rectangle region of Figures 6h and 7f,g,h. The imaging result has no obvious gap (Figure 7a,c,e) with the SSST result.

With simple energy accumulation criteria, the rigid body component can be roughly separated from the imaging results. The advantage of ST-based results (Figure 8b,d,f) relative to STFT (Figure 8a,c,e) is obvious. The former almost restored the details of the rigid part of the original model (Figure 3). It is worth mentioning that, although the contour of the rigid body part of the SSST2 imaging result is blurred at the rotational speeds of 10 r/s and 20/s (Figure 7c,e), the details of the extraction result can still be compared, with SST having a better performance (Figure 8d,f).

For the computing speed, SSST is not very different from the more complex SSST2, and the latter is even slightly faster (SSST: 1227s; SSST2: 934s). Moreover, due to the use of more matrix operations, SST is much faster than the other two methods (SST: 23s) that use more loop statements, as they hold similar levels of complexity. The above results show that there is still a lot of optimization space for the SSST and SSST2 programs used in this paper, and the calculation of operator (20) for SSST2 does not significantly change the computational complexity.



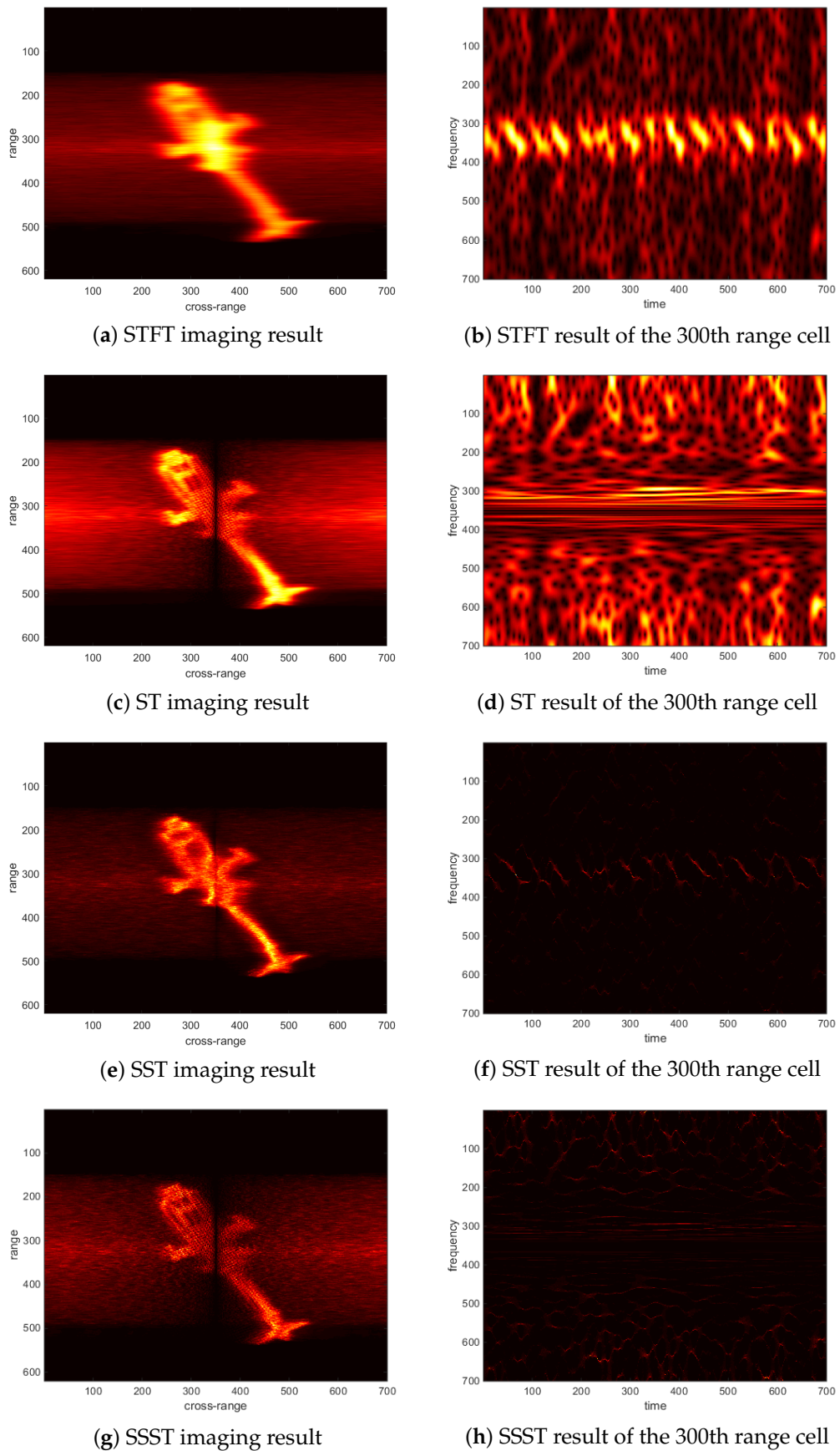


**Figure 4.** Results of target with a main rotor speed of 5 r/s. ST—S-transform; SST—synchrosqueezing transform; SSST—synchrosqueezing S-transform; STFT—short time Fourier transform.

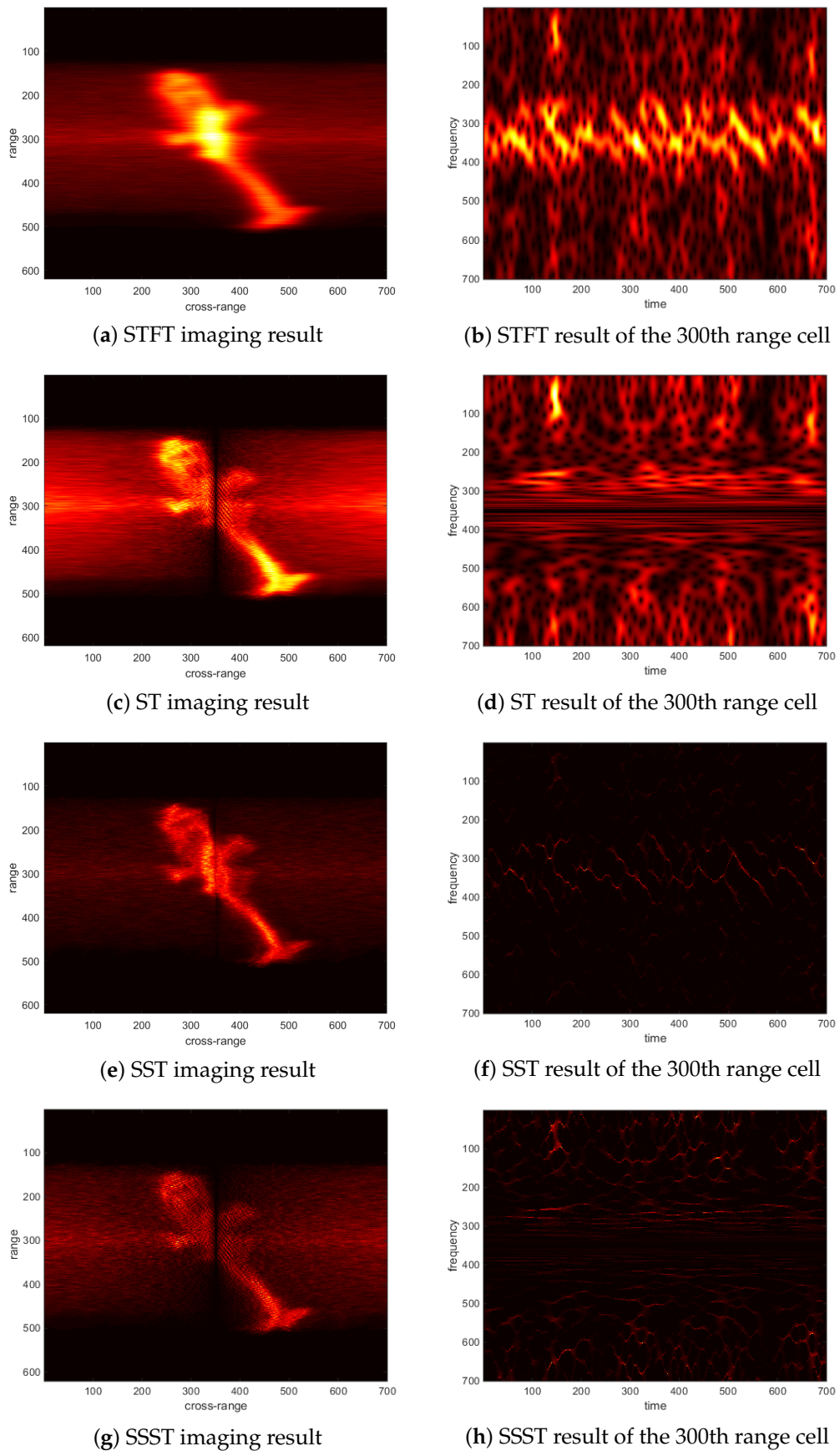


Figure 5. Results of target with a main rotor speed of 10 r/s.

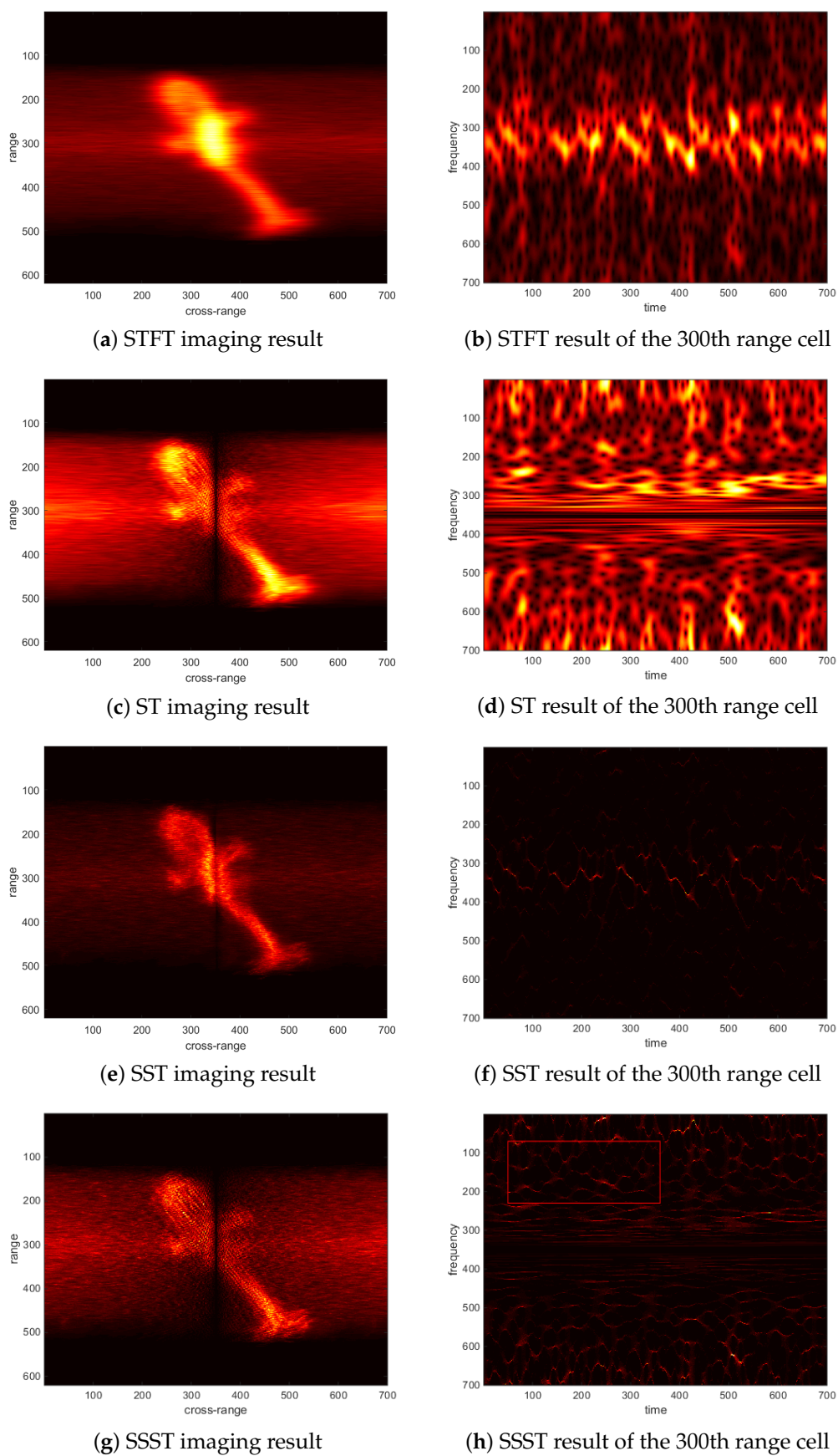
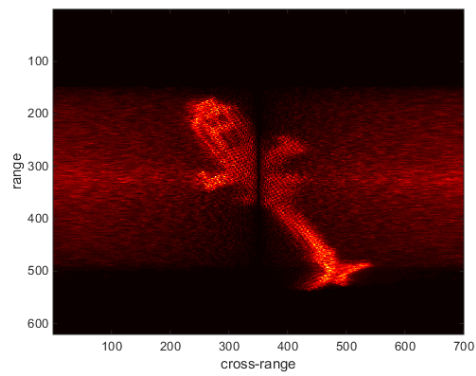
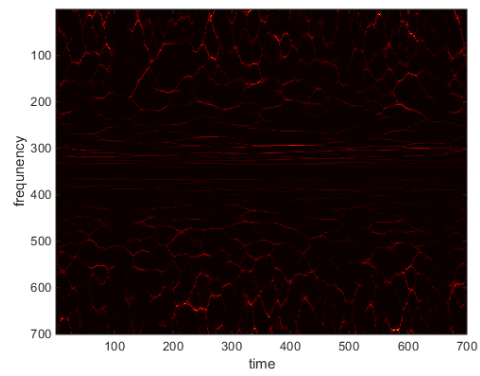


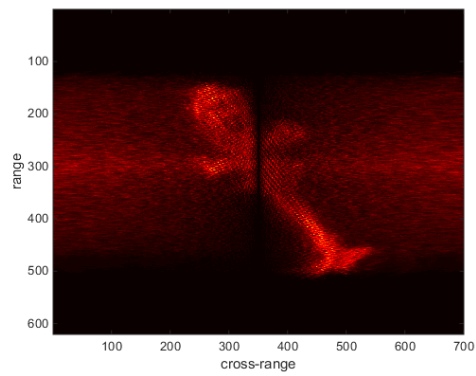
Figure 6. Results of target with a main rotor speed of 20 r/s.



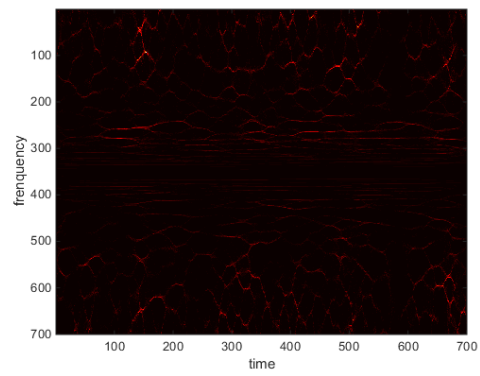
(a) SSST2 imaging result, 5 r/s



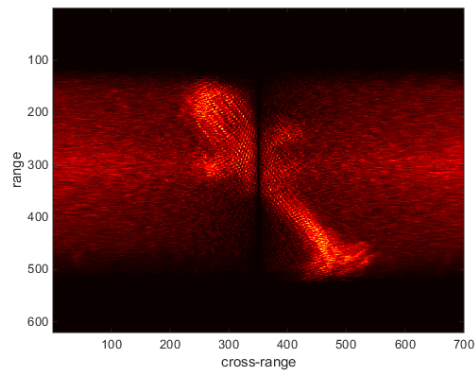
(b) SSST2 result of the 300th range cell, 5 r/s



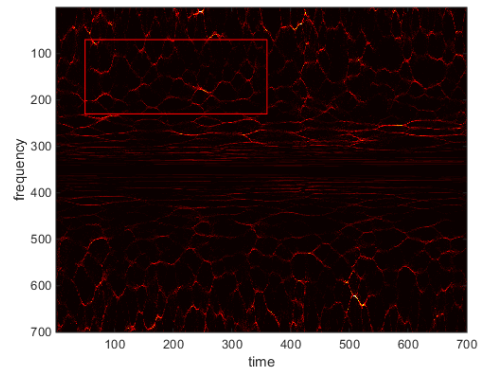
(c) SSST2 imaging result, 10 r/s



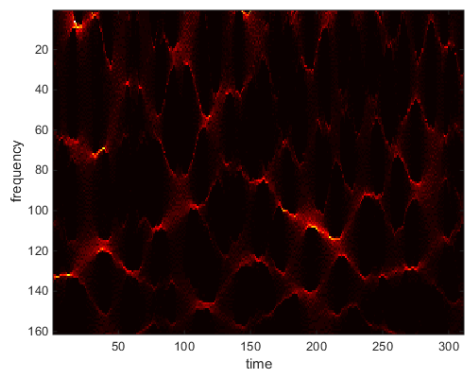
(d) SSST2 result of the 300th range cell, 10 r/s



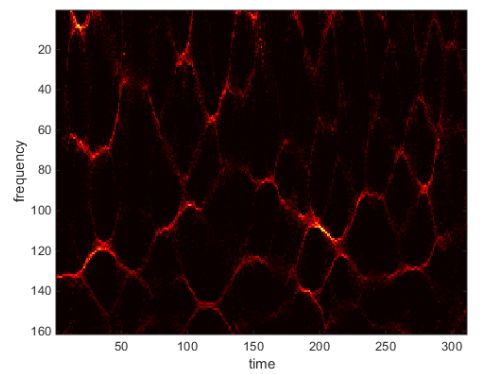
(e) SSST2 imaging result, 20 r/s



(f) SSST2 result of the 300th range cell, 20 r/s



(g) Zoom of the result of Figure 6g



(h) Zoom of the result of Figure 7f

**Figure 7.** Second-order synchrosqueezing S-transform (SSST2) results of target with different main rotor speed.

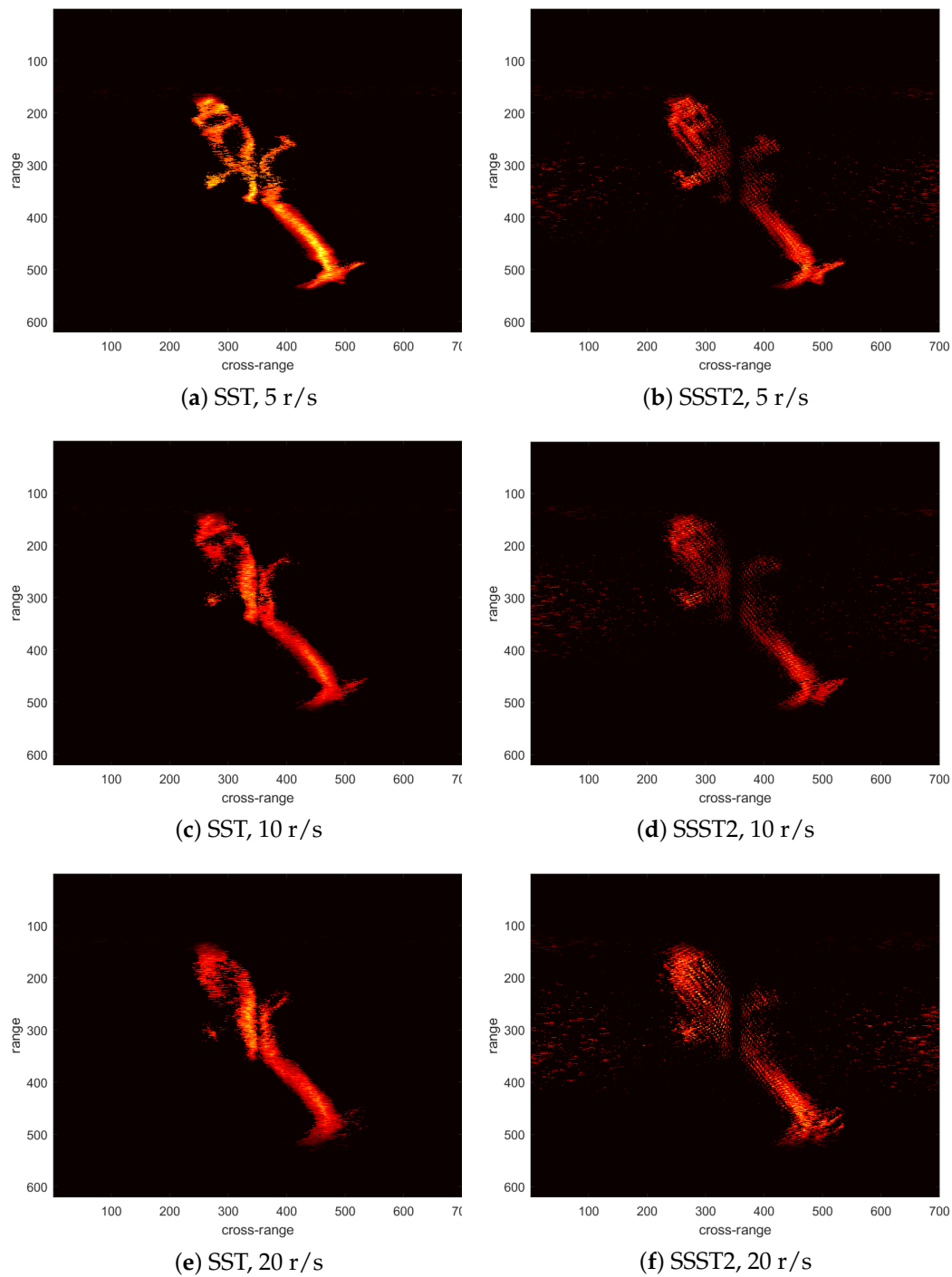
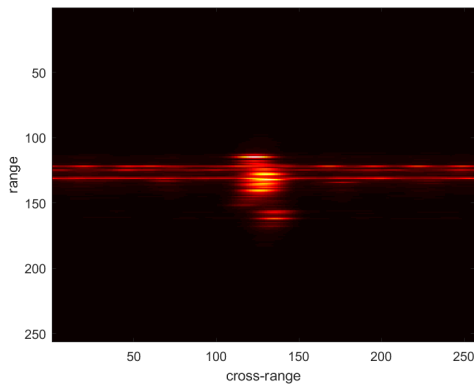


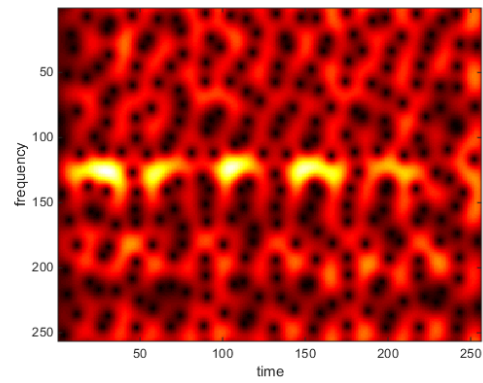
**Figure 8.** Imaging separation results of simulated signals.

Actual An-26 aircraft data is also subjected to similar experiments. Similar to Figures 4–6, Figure 9 shows the imaging effects of different methods (Figure 9a,c,e,g) and the time-frequency analysis results of a certain distance unit (Figure 9b,d,f,h). The difference between the results is still consistent with the previous simulation data. In addition, the imaging effects of SSST and SSST2 are still similar (Figures 9g and 10a), and their differences are reflected in the time resolution of high-frequency components (Figures 9h and 10b). For real data, STFT-based imaging is even worse; the more concentrated energy allows the latter to achieve a better separation result (Figure 11a,b).

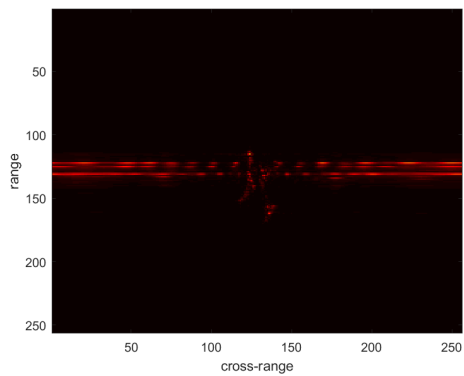




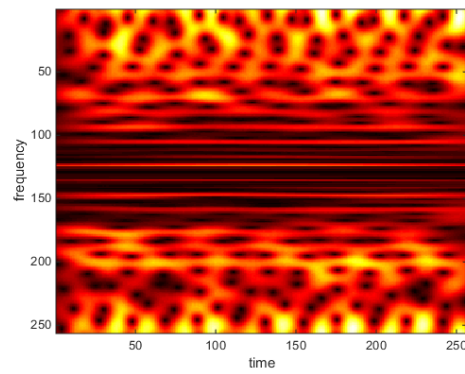
(a) STFT imaging result



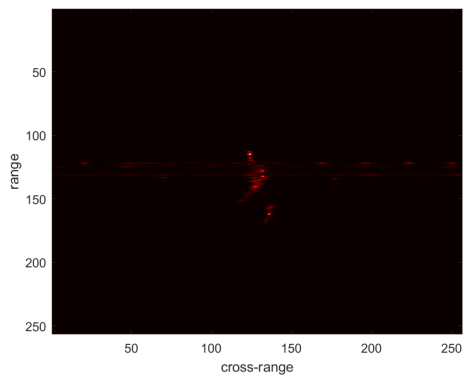
(b) STFT result of the 131st range cell



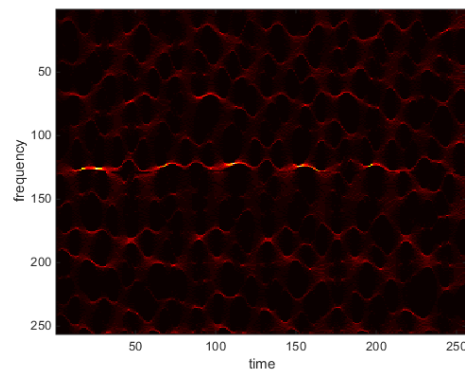
(c) ST imaging result



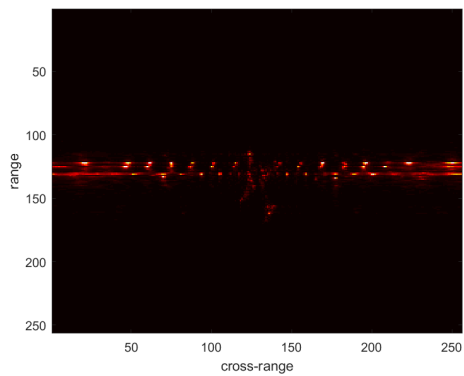
(d) ST result of the 131st range cell



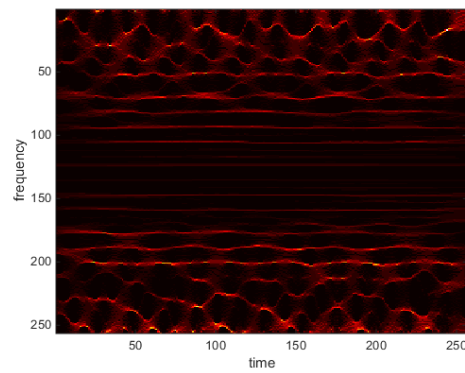
(e) SST imaging result



(f) SST result of the 131st range unit



(g) SSST imaging result



(h) SSST result of the 131st range unit

Figure 9. Time-frequency and imaging analysis results of real An-26 data.

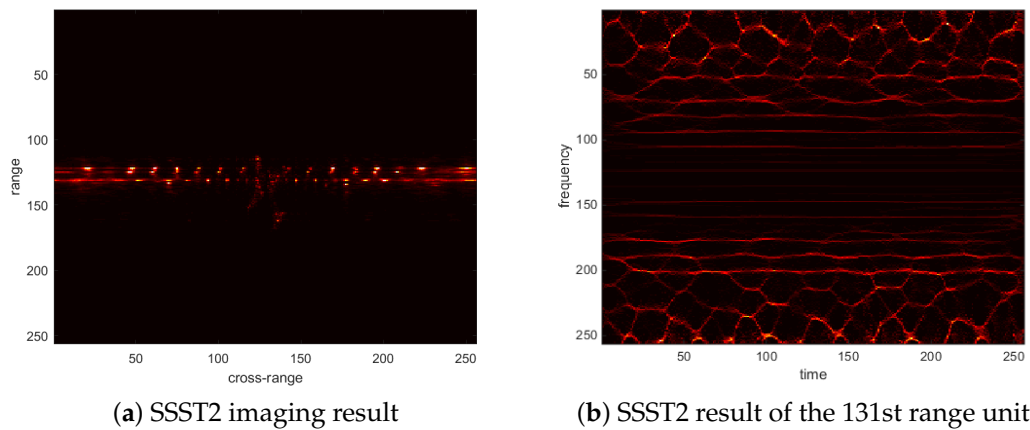


**Figure 10.** Time-frequency and imaging analysis results of real An-26 data.

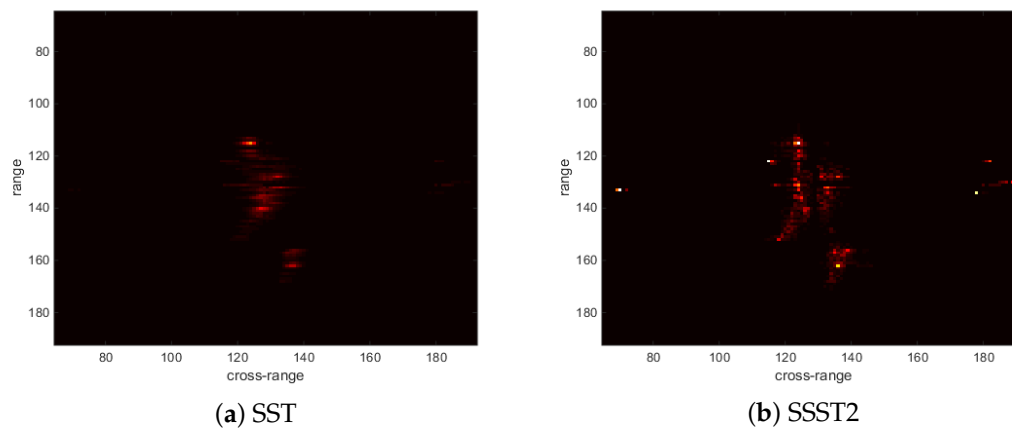


**Figure 11.** Imaging separation results of real An-26 data.

## 6. Conclusions

In this paper, S-transform is applied to ISAR imaging. Since the multiresolution characteristics of S-transform and the characteristics of radar echo signals match each other, better analysis and imaging results are achieved compared with STFT; this contrast is obvious in both simulation and actual data results. In the simulated helicopter model, although the micro-Doppler component brings more interference to the imaging results as the rotational speed of the rotor increases, after the application of the synchrosqueezing method, the quality of the time-frequency analysis results is significantly improved. Especially in the ST-based synchronous compression results, the change in the micro-Doppler component over time in the frequency direction is clearly depicted. All of the above will play an important role in subsequent work such as feature extraction, parameter estimation, etc.

**Author Contributions:** The contributions of the authors are as follows. Data curation, B.Z.; Formal analysis, M.Z.; Funding acquisition, X.Z.; Investigation, L.Z.

**Funding:** This research was funded by National Natural Science Foundation of China grant number 61701374.

**Conflicts of Interest:** The authors declare no conflict of interest.

## References

- Chen, V.C. Joint time-frequency analysis for radar signal and imaging. In Proceedings of the IEEE International Geoscience and Remote Sensing Symposium, Barcelona, Spain, 23–28 July 2007; pp. 5166–5169.
- Chen, V.C.; Li, F.; Ho, S.-S.; Wechsler, H. Analysis of micro-Doppler signatures. *IEEE Proc. Radar Sonar Navig.* **2003**, *150*, 271. [[CrossRef](#)]



3. Chen, V.C.; Li, F.; Ho, S.-S.; Wechsler, H. Micro-Doppler Effect in Radar: Phenomenon, Model, and Simulation Study. *IEEE Trans. Aerosp. Electron. Syst.* **2006**, *42*, 2–21. [[CrossRef](#)]
4. Luo, Y.; Zhang, Q.; Qiu, C.; Liang, X.; Li, K. Micro-Doppler Effect Analysis and Feature Extraction in ISAR Imaging With Stepped-Frequency Chirp Signals. *IEEE Trans. Geosci. Remote Sens.* **2010**, *48*, 2087–2098.
5. Stankovi'c, L.J.; Stankovi'c, S.; Thayaparan, T.; Dakovi'c, M.; Orovi'c, I. Separation and Reconstruction of the Rigid Body and Micro-Doppler Signal in ISAR Part I—Theory. *IET Radar, Sonar Navig.* **2015**, *9*, 1147–1154. [[CrossRef](#)]
6. Stankovi'c, L.J.; Stankovi'c, S.; Thayaparan, T.; Dakovi'c, M.; Orovi'c, I. Separation and Reconstruction of the Rigid Body and Micro-Doppler Signal in ISAR Part II—Statistical Analysis. *IET Radar Sonar Navig.* **2015**, *9*, 1155–1161. [[CrossRef](#)]
7. Stockwell, R.G.; Mansinha, L.; Lowe, R.P. Localization of the complex spectrum: The S transform. *IEEE Trans. Signal Process.* **1996**, *44*, 998–1001. [[CrossRef](#)]
8. Daubechies, I.; Lu, J.; Wu, H.T. Synchrosqueezed wavelet transforms: An empirical mode decomposition-like tool. *Appl. Comput. Harmon. Anal.* **2011**, *30*, 243–261. [[CrossRef](#)]
9. Brajovic, M.; Popovic-Bugarin, V.; Djurovic, I.; Djukanovic, S. Post-processing of Time-Frequency Representations in Instantaneous Frequency Estimation Based on Ant Colony Optimization. *Signal Process.* **2017**, *138*, 195–210. [[CrossRef](#)]
10. Oberlin, T.; Meignen, S.; Perrier, V. Second-Order Synchrosqueezing Transform or Invertible Reassignment? Towards Ideal Time-Frequency Representations. *IEEE Trans. Signal Process.* **2015**, *63*, 1335–1344. [[CrossRef](#)]
11. Pham, D.H.; Meignen, S. High-Order Synchrosqueezing Transform for Multicomponent Signals Analysis—With an Application to Gravitational-Wave Signal. *IEEE Trans. Signal Process.* **2017**, *65*, 3168–3178. [[CrossRef](#)]
12. Sejdic, E.; Djurovic, I.; Jiang, J. Time-frequency feature representation using energy concentration: An overview of recent advances. *Digit. Signal Process.* **2009**, *19*, 153–183. [[CrossRef](#)]
13. Huang, Z.; Zhang, J.; Zhao, T.; Sun, Y. Synchrosqueezing S-Transform and Its Application in Seismic Spectral Decomposition. *IEEE Trans. Geosci. Remote Sens.* **2016**, *54*, 817–825. [[CrossRef](#)]
14. Thakur, G.; Wu, H.T. Synchrosqueezing-based Recovery of Instantaneous Frequency from Nonuniform Samples. *Siam J. Math. Anal.* **2010**, *43*, 2078–2095. [[CrossRef](#)]
15. Auger, F.; Flandrin, P. Improving the readability of time-frequency and time-scale representations by the reassignment method. *IEEE Trans. Signal Process.* **1995**, *43*, 1068–1089. [[CrossRef](#)]
16. Daubechies, I.; Maes, S. A nonlinear squeezing of the continuous wavelet transform based on auditory nerve models. In *Wavelets in Medicine and Biology*; CRC Press: Boca Raton, FL, USA, 1996; pp. 527–546
17. Auger, F.; Flandrin, P.; Lin, Y.T.; McLaughlin, S.; Meignen, S.; Oberlin, T.; Wu, H.-T. Time-Frequency Reassignment and Synchrosqueezing: An Overview. *IEEE Signal Process. Mag.* **2013**, *30*, 32–41. [[CrossRef](#)]



© 2019 by the authors. Licensee MDPI, Basel, Switzerland. This article is an open access article distributed under the terms and conditions of the Creative Commons Attribution (CC BY) license (<http://creativecommons.org/licenses/by/4.0/>).